Colloids and Surfaces A 555 (2018) 365–371

Contents lists available at ScienceDirect

Colloids and Surfaces A

journal homepage: www.elsevier.com/locate/colsurfa

Dynamic contact angle hysteresis in liquid bridges

Zhang Shi[a], Yi Zhang[a], Mingchao Liu[a,b], Dorian A.H. Hanaor[c], Yixiang Gan[a,*]

[a] School of Civil Engineering, The University of Sydney, Sydney, NSW 2006, Australia
[b] Department of Engineering Mechanics, CNMM & AML, Tsinghua University, Beijing 100084, China
[c] Chair of Advanced Ceramic Materials, Technische Universität Berlin, Berlin 10623, Germany

GRAPHICAL ABSTRACT

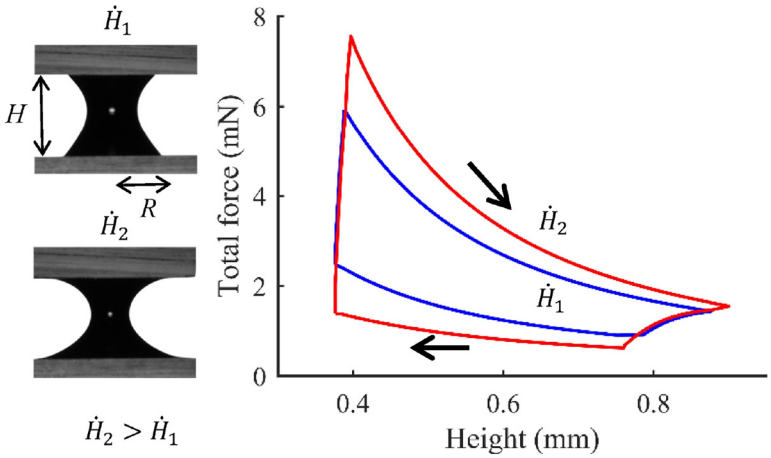

ARTICLE INFO

Keywords:
Contact angle hysteresis
Liquid bridges
Capillary number
Dynamic effects

ABSTRACT

This work presents an experimental study of dynamic contact angle hysteresis using liquid bridges under cyclic compression and stretching between two identical plates. Under various loading rates, contact angle hystereses for three different liquids were measured by examination of advancing and receding liquid bridges, and the capillary forces were recorded. It is found that for a given liquid, the hysteretic behaviour of the contact angle is more pronounced at higher loading rates. By unifying the behaviour of the three liquids, power-law correlations were proposed to describe the relationship between the dynamic contact angle and the capillary number for advancing and receding cases. It is found that the exponents of obtained power-law correlations differ from those derived through earlier methods (e.g., capillary rise), due to the different kinematics of the contact line. The various hysteretic loops of capillary force in liquid bridges under varied cyclic loading rates were also observed, which can be captured quantitatively by the prediction of our developed model incorporating the dynamic contact angle hysteresis. These results illustrate the importance of varying contact line geometries during dynamic wetting and dewetting processes, and warrant an improved modelling approach for higher level phenomena involving these processes, e.g., multiphase flow in porous media and liquid transfer between surfaces with moving contact lines.

* Corresponding author.
E-mail address: yixiang.gan@sydney.edu.au (Y. Gan).

https://doi.org/10.1016/j.colsurfa.2018.07.004
Received 12 April 2018; Received in revised form 29 June 2018; Accepted 2 July 2018
Available online 06 July 2018
0927-7757/ © 2018 Elsevier B.V. All rights reserved.

1. Introduction

Wetting and dewetting are fundamental processes in many applications, including inkjet printing [1], coating [2], lubrication [3], and soil science [4]. These applications usually involve dynamic conditions, e.g., drop impingement on substrates [5], requiring further consideration of the rate effects among multiple phases, i.e., gas, liquid and solid. Dynamic wetting and dewetting processes are characterised by the rate and state-dependent contact angle formed at the three-phase contact line, also known as the triple line. The interaction of these three phases at the contact line region governs contact angle dynamics [6].

When a droplet rests on a substrate, the formed contact angle varies and is limited by an upper value, namely the static advancing contact angle, θ_s^{adv}, and a lower value, namely the static receding contact angle, θ_s^{rec}. This behaviour is induced by surface roughness/heterogeneity [7] or surface forces acting in the vicinity of a contact line [8]. When the contact angle is between the two limiting values, the contact line is usually considered to be pinned and hysteretic behaviour can be observed. Beyond these two values, the contact line tends to move [9]. Under dynamic conditions, the contact angle is not only influenced by surface properties, but also the physical properties of fluid flow. Consequently, the utility of static contact angles to characterize wetting and dewetting is limited. When the contact line advances or recedes, velocity-governed dynamic advancing contact angles (θ_d^{adv}) or dynamic receding contact angles (θ_d^{rec}) will be observed, respectively [9]. Between these two dynamic values, rate-dependent dynamic contact angle hysteresis is observed.

Some theoretical works have attempted to explain the correlation between contact line velocities and dynamic contact angles using the hydrodynamic model [10,11] or the molecular-kinetic model [12,13]. In the hydrodynamic model, the contact line motion is dominated by the viscous dissipation, which provides a simple scaling relationship between the contact line motion in the form of Ca and a change in the contact angle as [10,11]

$$(\theta_d^3 - \theta_s^3) = 9\ln\left(\frac{L}{b}\right)\bullet Ca, \tag{1}$$

where θ_d is the dynamic contact angle, θ_s the static contact angle, and $\frac{L}{b}$ the ratio of the macroscopic to microscopic length scale. $Ca = v\mu/\gamma$ is the capillary number, where v is the contact line velocity, μ the viscosity of the liquid and γ the surface tension between air and liquid. However, this assumption neglects the surface characteristics near the contact line. In contrast, the molecular-kinetic model considers adsorption and desorption at the interface [12,13]. The dynamic contact angle is then related to the capillary number through the following equation:

$$(\cos\theta_s - \cos\theta_d) = \frac{2k_B T}{\lambda^2\gamma}\sinh^{-1}\left(\frac{Ca\bullet\gamma}{2k_0\lambda\mu}\right), \tag{2}$$

where k_B is the Boltzmann constant and T the temperature. k_0 and λ are two fitting parameters.

A number of master curves have been also developed empirically to describe dynamic angles, all of which express $(\cos\theta_s - \cos\theta_d)/(\cos\theta_s + 1)$ as a function of Ca, summarized in a general form as [14–17]

$$\frac{\cos\theta_s - \cos\theta_d}{\cos\theta_s + 1} = A\bullet Ca^B. \tag{3}$$

The correlation constant A ranges between 2 and 4.96 and the range of B is between 0.42 and 0.702 [14–17]. This correlation implies that the dynamic contact angle can be scaled by a universal relationship when $Ca < 0.01$. One of the first empirical correlations of this form was proposed by Jiang et al. [14], with values of A = 4.96 and B = 0.702, based on the data of capillary rise experiments carried out by Hoffman [18]. Another empirical correlation was presented by Bracke et al. [17], corresponding to values of A = 2 and B = 0.5, by considering the wetting of a vertical plane and the spreading of small drops. Both correlations of [14] and [17] show a good prediction of dynamic contact angles for $2 \times 10^{-3} < Ca < 3 \times 10^{-2}$ [15]. The empirical equation by Seebergh and Berg [15], having A = 4.47 and B = 0.42, was established by examining dynamic contact angles at lower capillary numbers ($10^{-7} < Ca < 10^{-3}$) via microtensiometry. Li et al. [16] also obtained an empirical correlation of the above form, with constants corresponding to A = 4.2 and B = 0.51, on the basis of capillary rise in micro pores. Overall, although no unique interpretation has been defined, correlation constants A and B are related to the analysis techniques, the range of Ca and geometric properties applied. It is important to note that empirical correlations were mostly obtained from advancing contact angles, and may not be applicable in receding cases.

Several experimental approaches to the measurement of dynamic contact angles have been implemented, including Wilhelmy plate [19,20], inclined surface [21], rotating cylinder [22,23], and capillary displacement techniques [16,24]. The experimental observations and theoretical equations are consistent, i.e., dynamic contact angles increase with increasing contact line velocities, while dynamic receding contact angles decrease with increasing velocities. As with the aforementioned theoretical models, these analyses were based on a fixed contact line length.

The kinematics of a contact line under liquid bridge conditions show different characteristics to the dynamic contact angle, i.e., even at a constant moving velocity, the geometry of contact line varies. In the context of liquid bridges, Chen et al. [25] investigated contact angle hysteresis during compression and stretching in quasi-static conditions between two flat substrates. However, the behaviour of a liquid bridge under dynamic conditions (e.g., dynamic contact angle hysteresis) remains unexplored. Radoev et al. [26] focused on the transition from static to dynamic states of liquid bridge during the rupture process. Pitois et al. [27] and Bozkurt et al. [28] studied capillary forces in liquid bridges between two identical spheres under varied separation velocities. But neither the evolution of contact angles nor capillary force hysteresis was considered. As the contact angle is an important parameter when the capillary force in a liquid bridge is calculated, the quasi-static capillary force hysteresis is a consequence of static contact angle hysteresis [29]. Under dynamic conditions, correlations between capillary force hysteresis and contact angle hysteresis have not yet been reported.

To date, few studies have examined dynamic wetting or dewetting processes using a liquid bridge with a varying contact line geometry. Here we report experiments where a liquid bridge is subjected to various cyclic loading rates between two flat substrates, in order to investigate the dynamic behaviour of contact angle hysteresis and capillary force hysteresis. By varying the displacement velocity, varied wetting and dewetting dynamics emerge, exhibiting contact angle hysteresis. We further analyse the contact line velocity from the experiments and present universal correlations for dynamic contact angles under a wide range of Ca values, for advancing and receding cases. The proposed correlations of dynamic contact angles facilitate the prediction of capillary forces arising from liquid bridges under dynamic conditions and are validated by experimentally observed dynamic capillary force hysteresis.

2. Experimental method

To measure the contact angle hysteresis, the advancing and receding angles in liquid bridges are extracted for different types of liquids under various cyclic loading rates, with simultaneous measurement of the capillary force.

2.1. Experimental setup

An advanced goniometer system (Rame-hart Model 200) was mounted on an anti-vibration honeycomb platform (HERZAN), including a high-speed camera, an illumination source, an analytical

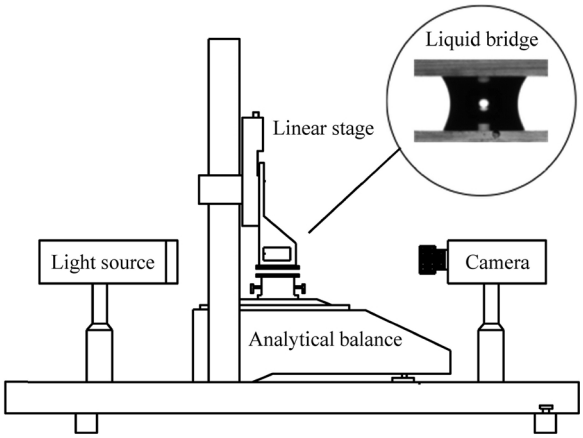

Fig. 1. Schematic representation of the experimental setup.

balance (A&D HR-250AZ), and a linear stage (Zaber Tech, T-LSM025A), as shown in Fig. 1. The goniometer was employed to image the contour of the moving meniscus between two parallel substrates at 30 frames per second. We placed an analytical balance beneath the bottom substrate to record the capillary force with an accuracy of 1 μN. The bottom substrate was placed on the stage mounted on the balance and the top substrate was fixed on the fixture attached to the linear stage, which was controlled by a computer at fixed speeds from 0.001 mm/s to 6 mm/s.

2.2. Material properties

Deionized water, 85% glycerol and 100% glycerol (Sigma-Aldrich) were used as wetting and dewetting fluids. 85% glycerol was prepared by mixing water and 100% glycerol. A micro syringe with an accuracy of 0.002 ml was applied to precisely control the droplet volume. Water and glycerol were chosen because of their similar surface tension, high affinity for each other and widely different viscosities. Table 1 lists the physical properties of liquids used in experiments, where ρ is the material density. To assess the influence of gravity, the capillary lengths for each liquid, calculated as $\lambda_c = \sqrt{\gamma/\rho g}$ where g is the gravitational acceleration, are given in Table 1.

Two identical glass substrates with an aminoalkylsilane coating (Sigma-Aldrich, S4651) were used as wetting surfaces, exhibiting reduced hydrophilicity relative to pristine glass. Prior to the experiments, they were thoroughly cleaned to ensure there was no contamination on the surface. The static contact angles for water, 85% glycerol and 100% glycerol on the tested surface were found to be 67.17 ± 1.46°, 65.08 ± 1.32° and 61.58 ± 0.78°, respectively, using the static sessile drop method. Substrates were firstly rinsed with pure water then with isopropyl alcohol. The glass substrates were then dried under vacuum for 2 min and immediately used to conduct the liquid bridge compression and stretching tests.

Table 1
The material and interfacial properties for the liquids used in the experiments.

	μ (g/cm s)[a]	γ (mN/m)[a]	ρ (g/cm^3)[a]	λ_c(mm)	θ_s^{adv}[b]	θ_s^{rec}[b]
Water	0.01	73	0.998	2.73	73°	59.5°
85% glycerol	1.09	65	1.221	2.38	59.5°	48°
100% glycerol	14.1	63	1.261	2.26	52°	51°

[a] The physical properties including viscosity, surface tension and density at 20 °C were obtained from literature data [30,31].

[b] Fitting parameters from the experimental data, see details in the discussion section.

2.3. Experimental procedure

A droplet was deposited by a syringe on the bottom glass substrate, with its volume confirmed by mass balance. The upper substrate was then moved toward the droplet to form a liquid bridge between the two parallel glass substrates. Several accommodation cycles were carried out prior to measurements to ensure the pre-wetting condition and an axisymmetric liquid bridge. Different upper substrate velocities were applied in the corresponding cycles. Images and capillary force were continuously recorded during the compression and stretching processes. All experiments were conducted under an ambient temperature of 20 ± 1 °C and humidity of 50%–60%.

As shown in the insert of Fig. 1, the liquid bridge has two contact angles on each surface. The difference between upper and lower contact angles due to gravity is of relevance only towards contact line hysteresis. That means that they are both equivalent for the comparable study presented here. Since contact angles on the lower surface may be influenced by gravity, only the two contact angles on the upper surface were measured and averaged. These were identified using parabolic fitting in a Matlab environment, with only the upper radii being measured for the calculation of contact-line velocities. To accurately measure the capillary force, the top substrate velocity was limited to a maximum of 0.2 mm/s owing to data acquisition rate limitations. The minimum velocity was set to 0.001 mm/s to reduce the effect of liquid evaporation during cyclic loadings. Due to the minimum loading rate applied, the travel distance of upper plate was controlled to be low to minimise the total time so that the volume loss due to the evaporation can be neglected.

3. Results and discussion

3.1. Dynamic contact angle hysteresis

Fig. 2 shows a liquid bridge (100% glycerol) in the receding stage under different applied velocities. It can be clearly seen that the receding contact angle monotonically decreases with increasing velocity, which demonstrates the dynamic effect on contact angles and the feasibility of this experimental method. Here, H is the height of liquid bridge; R is the contact radius; $\dot{H}$ is the velocity of the upper substrate.

In Fig. 3, typical dynamic contact angle hysteresis loops of water, 85% glycerol, and 100% glycerol are plotted against R under different $\dot{H}$. Four stages can be identified from the hysteretic loops, as indicated in the subfigures. Stage I to IV are the pinned stretching, receding, pinned compression and advancing stages, respectively. These hysteretic loops show that the increase of $\dot{H}$ results in a larger θ_d^{adv} but a smaller θ_d^{rec} in compression and stretching processes, respectively. The dynamic contact angle hysteresis, i.e., the difference between θ_d^{adv} and θ_d^{rec}, is greater for larger $\dot{H}$. Velocity dependence of contact angles arises from an interplay between two main factors, i.e., the capillary force and viscous force [32]. The capillary force due to surface tension decreases the dynamic contact angle hysteresis and the viscous force due to the viscosity increases the dynamic contact angle hysteresis [32]. As listed in Table 1, water, 85% and 100% glycerol exhibit similar magnitudes of surface tension but the viscosity of 100% glycerol is 10 times larger than that of 85% glycerol and more than 1000 times the viscosity of water. This explains why the dynamic contact angle hysteresis for 100% glycerol is largest for a given $\dot{H}$. These results show that the viscous force in this set of experiments greatly affects the dynamic contact angle hysteresis. Another observation made from Fig. 3 is that the contact radius is not completely fixed in pinning stages. This phenomenon is significant in stage III. The small shift represents non-equilibrium activities occurring at the vicinity of three-phase contact line, e.g., the micro-slip due to the presence of a thin film [8].

In order to develop a theoretical model to describe dynamic contact angles in liquid bridges, the contact line velocities correspond to the rate of change of the contact radius in the slipping stage, defined as

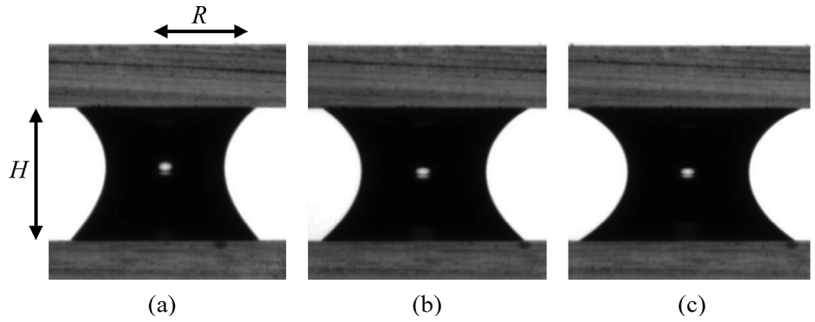

Fig. 2. Images of a liquid bridge at the same height (H = 2.125 mm) when the top substrate separate from the bottom one at (a) $\dot{H}$ = 0.02 mm/s, θ_d^{rec}= 46.62°; (b) $\dot{H}$ = 0.2 mm/s, θ_d^{rec}= 40.23°; (c) $\dot{H}$ = 2 mm/s, θ_d^{rec}= 34.75°.

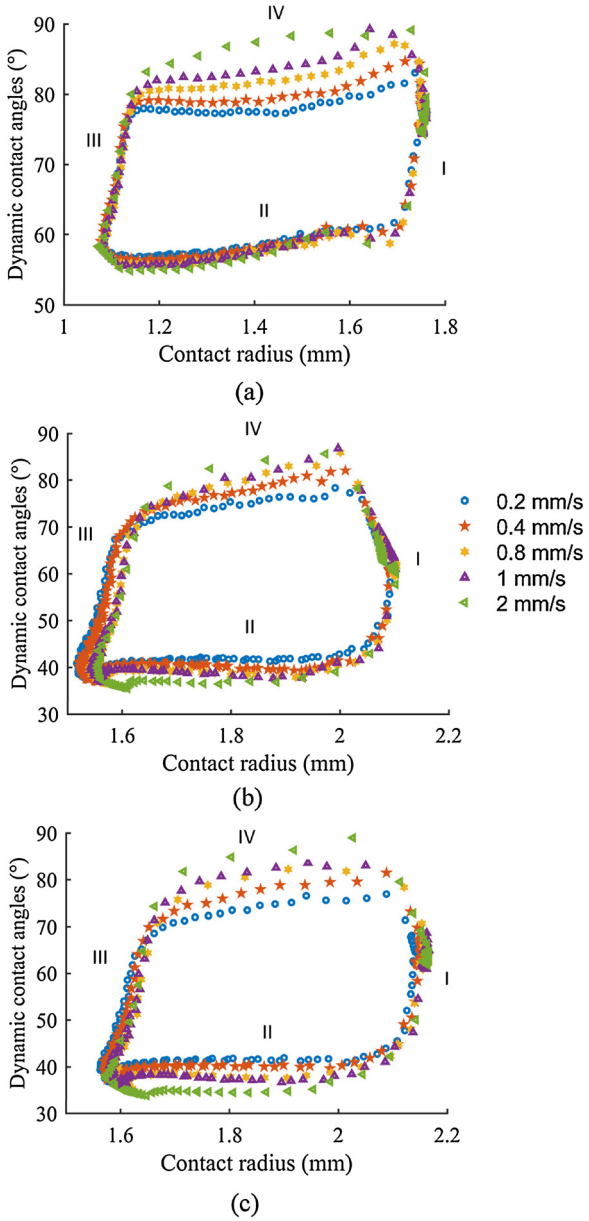

Fig. 3. Relation between contact radius and contact angle under different displacement velocities, $\dot{H}$ for: (a) water; (b) 85% glycerol; (c) 100% glycerol. Four stages can be identified: Stage I, pinned stretching; Stage II, the receding stage with the contact angle fluctuating around θ_d^{rec} and a receding contact line; Stage III, pinned compression; Stage IV, the advancing stage with the contact angle varying around θ_d^{adv} and the contact line advancing.

$\dot{R} = dR/dt$ where dR is the difference between upper radii of two consecutive frames, and dt is the time interval between each frame. Note that, for a given $\dot{H}$, the contact line velocity is not necessar ily equal to $\dot{H}$ and may vary during the slipping stages. Since, fewer data points are obtained with increasing velocity, for accuracy reasons $\dot{H}$ values of 0.02 mm/s, 0.04 mm/s, 0.1 mm/s, 0.2 mm/s, 0.4 mm/s and 0.8 mm/s are selected for this study.

In our experiments, the velocity v included in Ca is interpreted as the contact line velocity. A smooth probability density plot using $(cos\theta_d^{rec} - cos\theta_s^{rec})/(cos\theta_s^{rec} + 1)$ and Ca is made in Fig. 4a to represent the receding cases for three tested liquids. This format allows the application of the modified form of Eq. (3) to receding cases. For the advancing cases, a smooth probability density plot between $(cos\theta_s^{adv} - cos\theta_d^{adv})/(cos\theta_s^{adv} + 1)$ and Ca is presented in Fig. 4b. The actual probability can be calculated by integrating the corresponding probability density from the legend over the area. Based on the distribution behaviour seen in Fig. 4, power-law relationships can be found for the dynamic advancing and receding contact angles in liquid bridges, respectively, via least-square fitting, as

$$D_1 = \frac{cos\theta_d^{rec} - cos\theta_s^{rec}}{cos\theta_s^{rec} + 1} = 0.19Ca^{0.16} \quad (4)$$

$$D_2 = \frac{cos\theta_s^{adv} - cos\theta_d^{adv}}{cos\theta_s^{adv} + 1} = 0.52Ca^{0.17}. \quad (5)$$

Here, R^2 is 0.75 for the receding cases and R^2 is 0.84 for the advancing cases. Note that D_1 and D_2 are the dimensionless expressions of dynamic receding and advancing contact angles, respectively. Moreover, θ_s^{adv} and θ_s^{rec} of three liquids were obtained by fitting, which may bring some uncertainties compared to the static contact angle. These two contact angles are intrinsically and physically measurable, and can be directly obtained for $\dot{H}$ close to zero. It is interesting to find that D_1 and D_2 have similar power exponents through different loading phases.

For the advancing cases shown in Fig. 4b, when the contact line velocities of water and 85% glycerol are high, measured D_2 assumes a value higher than that of the proposed power-law relationship. That might be due to the experimental uncertainty in measuring angles on both sides of the liquid bridge. When the contact angle for the advancing case approaches 90°, parabolic fitting can result in greater measurement errors. In should be noted that pre-existing thin films of liquid on the substrates can slightly increase the contact angle.

Our results are scaled by using Ca, which demonstrates a good power-law relationship with only two fitting parameters for either advancing or receding cases. These newly developed power-law correlations can predict dynamic contact angles in liquid bridges for advancing and receding cases over a wide capillary number regime ($10^{-7} < Ca < 10^{-2}$). This represents a first attempt to apply the modified form of Eq. (3) to receding cases. In comparison to the hydrodynamic model and molecular-kinetic model, different liquids for both advancing and receding cases need to be fit by different sets of parameters.

It is noted that the constants found in our new correlations differ

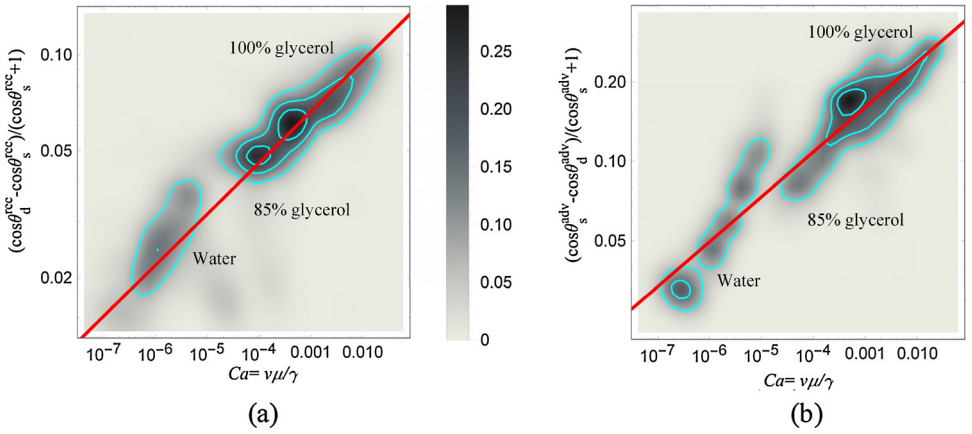

Fig. 4. Effect of *Ca* on dynamic contact angles: (a) θ_d^{rec} and (b) θ_d^{adv} of water, 85% and 100% glycerol under varied velocities, with the solid red lines as proposed correlations as a comparison. (For interpretation of the references to color in this figure legend, the reader is referred to the web version of this article).

significantly from those derived from earlier techniques, in particular the exponent in the power-law relationship. The range of the power-law exponents in previous models is between 0.42 and 0.702 [14–17], while the exponents obtained here are significantly smaller than the lower limit of this range. One reason is due to different kinematics of contact line. Jaehyunk et al. [33] adopted the modified Wilhemply plate method to measure the wettability of irregular shapes and demonstrated that the wetting length is important in determining the contact angle. However, in previous techniques, namely the capillary rise and the Wilhelmy plate, to measure dynamic contact angles and obtain the empirical equation, the contact line conducts a one-dimensional motion, i.e., the length of the contact line remains constant. Thus, the energy dissipation per unit length can be considered as a constant. In our experiments, when a liquid bridge is compressed or stretched, the contact line undergoes a radial movement. That is, the length of the contact line keeps changing, which results in the modification of the energy dissipation rate during the wetting and dewetting processes. Thus, we assume that the power-law exponent in the empirical correlation is associated with the kinematics of the contact line, which requires controlled experiments to quantify. Another main reason is the nature of flow that tends to affect the dynamic contact angle for forced wetting. Simulations carried out by Blake et al. [34] demonstrated that the large shear stresses generated in liquid bridges cause large slip velocities and give rise to an additional driving force. Similarly, in our experiments, the shear stress induced by the compression and stretching of liquid bridges, brings about noticeable slip velocities, $\dot{R}_{slip} > 0$. In other words, the measured contact line velocity in experiments is larger than the effective contact line velocity as $\dot{R} - \dot{R}_{slip}$. For smaller contact line velocities, fitting using the format of Eqs. (5) and (6) will result in a larger power law exponent.

3.2. Capillary force hysteresis

Within the experiments, the force hysteresis in a dynamic liquid bridge is influenced by dynamic contact angles. The measured total force can be decomposed into the capillary force and viscous force as

$$F_t = F_c + F_v \tag{6}$$

where F_t is the total force, F_c is the capillary force, and F_v is the viscous force opposite to the movement of the upper substrate [27]. A positive total force indicates the parallel substrates are attracted by the liquid bridge, while repulsion is associated with a negative total force.

Fig. 5 shows the variation of the total-force hysteresis for water, 85% glycerol, and 100% glycerol under various cyclic loading rates. It is clear that four stages can be identified in these figures, corresponding to these in Fig. 3. It is noted that at a given separation H, F_t in the stretching process is larger than that in the compression process, which

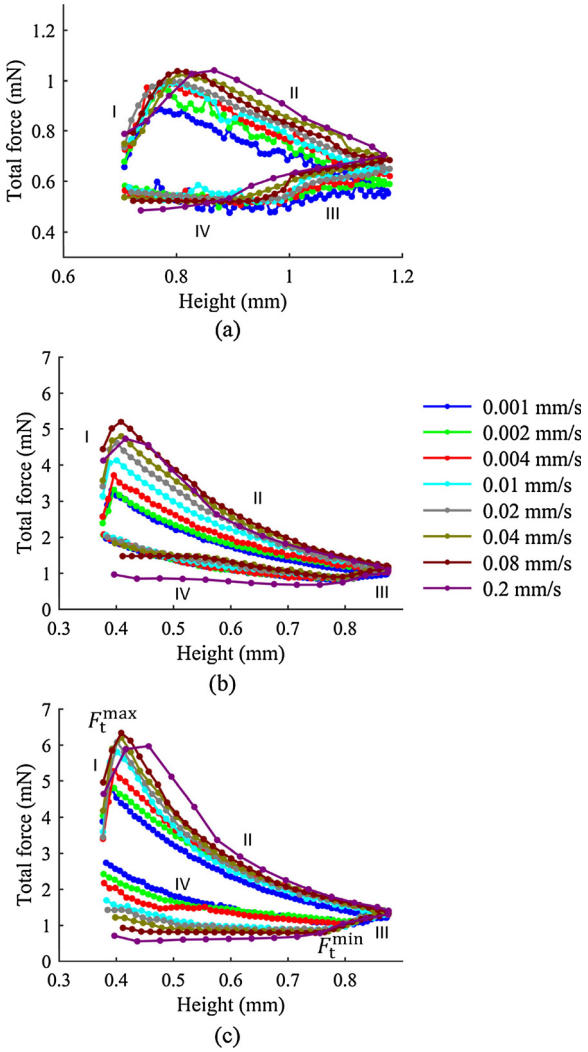

Fig. 5. Variation of total-force versus height under different $\dot{H}$ for (a) water; (b) 85% glycerol; (c) 100% glycerol. Four stages are observed through the cyclic loading, corresponding to these in Fig. 3.

demonstrates the hysteretic phenomenon. Varying force hysteretic loops (see Fig. 5) were observed under different cyclic loading rates. It is clearly seen that the total-force hysteresis becomes more significant with increasing $\dot{H}$.

Contact line velocities affect dynamic contact angle hysteresis, i.e.,

the contact angle is limited by the θ_d^{adv} and θ_d^{rec} instead of θ_s^{adv} and θ_s^{rec} in the dynamic condition. Since the profile of a liquid bridge governs the capillary pressure, the capillary pressure tends to vary with contact angle hysteresis, thus influencing the force hysteresis. As the viscous force doesn't exhibit strong hysteresis and the static liquid bridge force-displacement curve is directly related to the contact angle hysteresis [25,35], it can be concluded that the observed hysteresis of the total force-height curve in our experiments is predominantly caused by dynamic contact angle hysteresis.

Additionally, a maximum value of total force, F_t^{max}, can be found during the stretching process while a minimum value of total force, F_t^{min}, can be found during the compression process. With increasing $\dot{H}$, F_t^{max} and F_t^{min} increase and decrease, respectively. For $\dot{H} = 0.2$ mm/s, F_t^{max} could not be detected due to data acquisition limitations. This behaviour is also determined by dynamic contact angle hysteresis. F_t^{max} can be found when the contact angle transitions to its receding value and F_t^{min} can be found when its advancing value is attained.

One interesting observation from the results shown in Fig. 5 is that, when $\dot{H}$ is large enough, F_t remains nearly unchanged or even decreases in stage IV. The viscous term F_v from the liquid bridge is proportional to $\dot{H}$ [36] and F_v acts in opposite direction to F_c in this situation. If the $\dot{H}$ is large enough, the increase of F_c due to the decreasing height is completely countervailed by the increasing contribution of F_v.

To compare the capillary length (as shown in Table 1) with the corresponding characteristic length scale in our experiments, the maximum height of liquid bridges was set as 2.37 mm, 2.95 mm and 2.85 mm for water, 85% and 100% glycerol, respectively. Thus, only the liquid bridge at the near end of stretching process and the commencement of compression process ($H \geq \lambda_c$) slightly experienced gravity effect. However, the contact angle hysteresis is the main focus in this study, and primarily governed by the characteristics at the local contact line region. Though gravity tends to affect the overall profile of liquid bridge, the local contact angle dynamics is not necessarily associated with the gravity condition, as evidenced by previous studies under the equilibrium state [37].

3.3. Modified capillary force model with dynamic contact angle hysteresis

For the purpose of predicting the total force under dynamic conditions, a modified theoretical model incorporating the newly developed correlation of dynamic angles is established. We start with the prediction of capillary forces under dynamic conditions. The static or quasi-static capillary forces between two plates have been extensively studied [25,26,38]. Our model extends the classical capillary force model to the dynamic case by considering the variation of the contact angle in the slipping stage. That is, the contact angle in our modified capillary force model is not fixed but changes with respect to the contact-line velocity. The profile of the liquid bridge is assumed to be axisymmetric and is determined by the Young-Laplace equation [27]

$$\frac{\Delta p}{\gamma} = 2C = \frac{r(z)''}{(1 + r(z)')^{\frac{3}{2}}} - \frac{1}{z(1 + r(z)')^{\frac{1}{2}}} \tag{7}$$

Here, $\Delta p = u_v - u_l$ is the capillary pressure, where u_v and u_l are the pressure outside and inside the liquid bridge, respectively, C is the mean curvature, and $r(z)$ is the profile of the meniscus determined by the contact radius, R, contact angle, θ and liquid bridge height, H. For simplicity here, a circular meniscus geometry is assumed so that Eq. (7) can be expressed in terms of R, θ and H. Then, the capillary force is estimated at the contact line point

$$F_c = 2\pi R\gamma \sin\theta + \pi R^2 \Delta p \tag{8}$$

To solve Eq. (8), the shape of the liquid bridge (R, θ and H) at each time point needs to be computed. The volume of the liquid bridge, V is (assuming $z = 0$ at the centre of a liquid bridge)

$$V = \pi \int_{-\frac{H}{2}}^{\frac{H}{2}} r(z)^2 dz \tag{9}$$

Considering mass conservation, the total derivative of Eq. (9) becomes

$$\frac{dV}{dt} = \frac{\partial V}{\partial R}\cdot\dot{R} + \frac{\partial V}{\partial \theta}\cdot\dot{\theta} + \frac{\partial V}{\partial H}\cdot\dot{H} = 0. \tag{10}$$

In the pinning stage, R is fixed so that $\dot{R} = 0$. Considering $\dot{H}$ is a control parameter, $\dot{\theta}$ can be uniquely determined by substituting Eq. (9) into Eq. (10). Then, the evolution of R, θ and H in the pinning stage over time can be obtained. In the slipping stage, there is a simple relationship between the contact line velocity, $\dot{R}$ and θ, which can be obtained from Eqs. (4) or (5) depending on whether the advancing or receding case is considered so that the rate of change of R can be expressed as a general form

$$\dot{R} = g(\theta) \tag{11}$$

Combining with Eqs. (9)–(11), the evolution of R, θ and H in the slipping stage over time can be derived via iterations. Substituting the evaluated parameters, i.e., R, θ and H, into Eq. (7) one can obtain the capillary pressure and F_c is obtained via using Eq. (8).

Regarding the prediction of the viscous force, it can be estimated based on the area in the centre plane of the meniscus as [36]

$$F_v = -\dot{H} R_n^4 \frac{3\pi\mu}{2H^3} \tag{12}$$

where R_n is the neck radius of the capillary bridge (in the range of 1.3 mm to 2.7 mm in this study). Regarding the contribution of the viscous force, it can reach up to 20% of the capillary force for 100% glycerol at the minimum height of liquid bridge and $\dot{H} = 0.2$ mm/s. Thus, the total force is the sum of the capillary force from Eq. (8) and the viscous force from Eq. (12). It should be noted that the transition point from pinning to slipping stages cannot be captured in this model. However, this doesn't affect the overall hysteretic loops of the capillary force and the idea here is to demonstrate the rate effect on the slipping stage.

As the rate effect on bridges of 100% glycerol is more significant compared with water and 85% glycerol (See Fig. 5), the prediction for force hysteresis in 100% glycerol is conducted using the above theoretical model. Fig. 6 shows the comparison of the predicted total force against experimental results for 100% glycerol, showing a good quantitative agreement. The droplet volume of 100% glycerol corresponded to that of the experiment, 8.2 ± 0.08 μl. The discrepancy between the

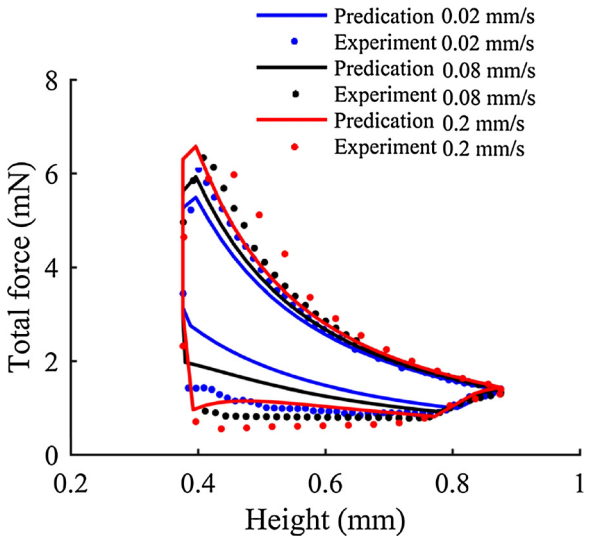

Fig. 6. Comparison of experimental results with the model prediction for 100% glycerol at (a): $\dot{H} = 0.02$ mm/s; (b): $\dot{H} = 0.08$ mm/s; (c): $\dot{H} = 0.2$ mm/s.

predicted and experimental results could be due to errors from two aspects. Firstly, using parabolic fitting to identify the contact angle may introduce some measurement errors, leading to the variation of the obtained power-law relationship (Eqs. (4) and (5)). Secondly, in the model, the meniscus is assumed to be circular in shape so that the constant mean curvature is not achieved when the capillary pressure is analysed. Despite slight discrepancies, a relatively good agreement is found between predictions and experimental data, and it can be stated that the developed model captures overall force hysteresis and rate effects on liquid bridge forces.

The results presented here facilitate an improved understanding of wet adhesion under dynamic effects. For a system including a single liquid bridge being stretched and compressed, the maximum adhesion, F_t^{max}, is determined by θ_d^{rec}, and the minimum adhesion, F_t^{min}, is associated with θ_d^{adv}. Here, both θ_d^{rec} and θ_d^{adv} depend on the applied loading rate. Additionally, the new correlations of dynamic contact angles can be adopted into the realm of unsaturated soils. The movement speed of a meniscus at the microscopic scale controls the contact angle that can greatly affect the soil water retention curves in unsaturated soils [39].

4. Conclusion

This work presents the first experimental and theoretical study of dynamic contact angle hysteresis in liquid bridges. Liquid bridge stretching and compression experiments were carried out to investigate the dynamic effect on contact angle hysteresis. Varied cyclic loading rates generate different hysteretic loops of dynamic contact angles. It is found that θ_d^{adv} increases and θ_d^{rec} decreases, with an increase in bridge displacement velocity, $\dot{H}$. Based on the variation of θ_d^{adv} and θ_d^{rec} under various contact line velocities, new correlations have been proposed to quantitatively describe the dynamic contact angle for advancing and receding cases, respectively. The obtained new power-law exponent differs from earlier models and may be related to contact line kinematics. We present here for the first time an adaptation of the general form expression for the correlation of dynamic contact angles, to receding cases. In relation to existing techniques for the study of dynamic contact angles, an important new aspect of this work is the inclusion of radial contact line movement.

Importantly, the dynamic contact angle hysteresis is found to have a significant effect on hysteretic capillary forces arising from the liquid bridge. A physical model incorporating the new correlations of dynamic contact angles has been established to predict the dynamic capillary force in liquid bridges. The model predictions of capillary force under dynamic conditions quantitatively reproduce the observed behaviour of liquid bridges. The experimental data, correlations and modified capillary force model presented here can be used to predict the dynamic behaviour of liquid bridges, relevant to a range of industrial applications. These results illustrate the importance of varying contact line geometries during dynamic wetting and dewetting, and warrant an improved modelling approach for these processes. To quantitatively establish the correlation to the varying contact line, further controlled experiments can be conducted in the future, such as the capillary rise in conical shaped tubes.

Acknowledgements

The authors are grateful for the financial support from Australian Research Council (Projects DE130101639 and DP170102886) and The University of Sydney SOAR Fellowship.

References

[1] B.-J. de Gans, P.C. Duineveld, U.S. Schubert, Inkjet printing of polymers: state of the art and future developments, Adv. Mater. 16 (2004) 203–213.
[2] L. Introzzi, J.M. Fuentes-Alventosa, C.A. Cozzolino, S. Trabattoni, S. Tavazzi, C.L. Bianchi, A. Schiraldi, L. Piergiovanni, S. Farris, “Wetting enhancer” pullulan coating for antifog packaging applications, ACS Appl. Mater. Interfaces 4 (2012) 3692–3700.
[3] Z. Pawlak, A.D. Petelska, W. Urbaniak, K.Q. Yusuf, A. Oloyede, Relationship between wettability and lubrication characteristics of the surfaces of contacting phospholipid-based membranes, Cell Biochem. Biophys. 65 (2013) 335–345.
[4] V.A. Kholodov, N.V. Yaroslavtseva, M.A. Yashin, A.S. Frid, V.I. Lazarev, Z.N. Tyugai, E.Y. Milanovskiy, Contact angles of wetting and water stability of soil structure, Eurasian Soil Sci. 48 (2015) 600–607.
[5] M. Remer, M. Psarski, K. Gumowski, J. Rokicki, G. Sobieraj, M. Kaliush, D. Pawlak, G. Celichowski, Dynamic water contact angle during initial phases of droplet impingement, Colloids Surf. A Physicochem. Eng. Asp. 508 (2016) 57–69.
[6] L. Gao, T.J. McCarthy, How Wenzel and Cassie were wrong, Langmuir 23 (2007) 3762–3765.
[7] J.F. Joanny, P.G. de Gennes, A model for contact angle hysteresis, J. Chem. Phys. 81 (1984) 552–562.
[8] I.V. Kuchin, V.M. Starov, Hysteresis of the contact angle of a meniscus inside a capillary with smooth, homogeneous solid walls, Langmuir 32 (2016) 5333–5340.
[9] H.B. Eral, D.J.C.M.’t Mannetje, J.M. Oh, Contact angle hysteresis: a review of fundamentals and applications, Colloid Polym. Sci. 291 (2013) 247–260.
[10] R.G. Cox, The dynamics of the spreading of liquids on a solid surface. Part 1. Viscous flow, J. Fluid Mech. 168 (1986) 169–194.
[11] O.V. Voinov, Hydrodynamics of wetting, Fluid Dyn. 11 (1976) 714–721.
[12] T.D. Blake, J.M. Haynes, Kinetics of liquid/liquid displacement, J. Colloid Interface Sci. 30 (1969) 421–423.
[13] T.D. Blake, The physics of moving wetting lines, J. Colloid Interface Sci. 299 (2006) 1–13.
[14] T.-S. Jiang, O. Soo-Gun, J.C. Slattery, Correlation for dynamic contact angle, J. Colloid Interface Sci. 69 (1979) 74–77.
[15] J.E. Seebergh, J.C. Berg, Dynamic wetting in the low capillary number regime, Chem. Eng. Sci. 47 (1992) 4455–4464.
[16] X. Li, X. Fan, A. Askounis, K. Wu, K. Sefiane, V. Koutsos, An experimental study on dynamic pore wettability, Chem. Eng. Sci. 104 (2013) 988–997.
[17] M. Bracke, F. De Voeght, P. Joos, The kinetics of wetting: the dynamic contact angle, Trends Colloid Interface Sci. III vol. 79, (1989), pp. 142–149.
[18] R.L. Hoffman, A study of the advancing interface I. Interface shape in liquid-gas systems, J. Colloid Interface Sci. 50 (1975) 228–241.
[19] X. Wang, Q. Min, Z. Zhang, Y. Duan, Y. Zhang, J. Zhai, Influence of head resistance force and viscous friction on dynamic contact angle measurement in Wilhelmy plate method, Colloids Surf. A Physicochem. Eng. Asp. 527 (2017) 115–122.
[20] A. Mohammad Karim, H.P. Kavehpour, Effect of viscous force on dynamic contact angle measurement using Wilhelmy plate method, Colloids Surf. A Physicochem. Eng. Asp. 548 (2018) 54–60.
[21] N. Le Grand, A. Daerr, L. Limat, Shape and motion of drops sliding down an inclined plane, J. Fluid Mech. 541 (2005) 293–315.
[22] F. Henrich, D. Fell, D. Truszkowska, M. Weirich, M. Anyfantakis, T.-H. Nguyen, M. Wagner, G.K. Auernhammer, H.-J. Butt, Influence of surfactants in forced dynamic dewetting, Soft Matter 12 (2016) 7782–7791.
[23] D. Fell, G. Auernhammer, E. Bonaccurso, C. Liu, R. Sokuler, H.-J. Butt, Influence of surfactant concentration and background salt on forced dynamic wetting and dewetting, Langmuir 27 (2011) 2112–2117.
[24] A. Siebold, M. Nardin, J. Schultz, A. Walliser, M. Oppliger, Effect of dynamic contact angle on capillary rise phenomena, Colloids Surf. A Physicochem. Eng. Asp. 161 (2000) 81–87.
[25] H. Chen, A. Amirfazli, T. Tang, Modeling liquid bridge between surfaces with contact angle hysteresis, Langmuir 29 (2013) 3310–3319.
[26] B. Radoev, I.T. Ivanov, P. Petkov, Capillary bridge: transition from equilibrium to hydrodynamic state, Colloids Surf. A Physicochem. Eng. Asp. 505 (2016) 98–105.
[27] O. Pitois, P. Moucheront, X. Chateau, Liquid bridge between two moving spheres: an experimental study of viscosity effects, J. Colloid Interface Sci. 231 (2000) 26–31.
[28] M.G. Bozkurt, D. Fratta, W.J. Likos, Capillary forces between equally sized moving glass-beads: an experimental study, Can. Geotech. J. 54 (2017) 1300–1309.
[29] C.D. Willett, M.J. Adams, S.A. Johnson, J.P.K. Seville, Effects of wetting hysteresis on pendular liquid bridges between rigid spheres, Powder Technol. 130 (2003) 63–69.
[30] J. Segur, G.P. Association, Physical properties of glycerine and its solutions, Glycerine Producers’ Association, 1963, pp. 1–27.
[31] K.A. Sharp, ELS (Ed.), Water: Structure and Properties, John Wiley & Sons, Ltd, 2001.
[32] S.P. Friedman, Dynamic contact angle explanation of flow rate-dependent saturation-pressure relationships during transient liquid flow in unsaturated porous media, J. Adhes. Sci. Technol. 13 (1999) 1495–1518.
[33] J. Park, U. Pasaogullari, L. Bonville, Wettability measurements of irregular shapes with Wilhelmy plate method, Appl. Surf. Sci. 427 (2018) 273–280.
[34] T.D. Blake, J.-C. Fernandez-Toledano, G. Doyen, J. De Coninck, Forced wetting and hydrodynamic assist, Phys. Fluids 27 (2015) 112101.
[35] E.J. De Souza, L. Gao, T.J. McCarthy, E. Arzt, A.J. Crosby, Effect of contact angle hysteresis on the measurement of capillary forces, Langmuir 24 (2008) 1391–1396.
[36] B. Bhushan, Adhesion, Introd. to Tribol. John Wiley & Sons, Ltd, 2013, pp. 157–198.
[37] H. Fujii, H. Nakae, Effect of gravity on contact angle, Philos. Mag. A 72 (1995) 1505–1512.
[38] P. Lambert, J.-B. Valsamis, P. Lambert (Ed.), Axial Capillary Forces BT - Surface Tension in Microsystems: Engineering Below the Capillary Length, Springer Berlin Heidelberg, Berlin, Heidelberg, 2013, pp. 19–44.
[39] Z. Liu, X. Yu, L. Wan, Influence of contact angle on soil–water characteristic curve with modified capillary rise method, Transp. Res. Rec. J. Transp. Res. Board 2349 (2013) 32–40.